

Electronic, magnetic, and vibrational properties of the molecular magnet Mn_4 monomer and dimer

Kyungwha Park ^{a,b} Mark R. Pederson ^{a,*} Noam Bernstein ^a

^a*Center for Computational Materials Science, Code 6390, Naval Research Laboratory, Washington DC 20375*

^b*Department of Electrical Engineering and Materials Science Research Center, Howard University, Washington DC 20059*

Abstract

A new type of the single-molecule magnet $[\text{Mn}_4\text{O}_3\text{Cl}_4(\text{O}_2\text{CEt})_3(\text{py})_3]$ forms dimers. Recent magnetic hysteresis measurements on this single-molecular magnet revealed interesting phenomena: an absence of quantum tunneling at zero magnetic field and tunneling before magnetic field reversal. This is attributed to a significant antiferromagnetic exchange interaction between different monomers. To investigate this system, we calculate the electronic structure, magnetic properties, intramolecular and intermolecular exchange interactions using density-functional theory within the generalized-gradient approximation. Our calculations agree with experiment. We also calculate vibrational infrared absorption and Raman scattering intensities for the monomer which can be tested experimentally.

Key words: single-molecule magnet, quantum tunneling, antiferromagnetic exchange interaction, density-functional theory

PACS: 75.50.Xx, 75.45.+j, 75.30.Gw, 75.30.Et

1 Introduction

Single-molecule magnets (SMMs) are three-dimensional arrays of identical nanoscale molecules, each of which consists of several transition metal ions surrounded by organic ligands. These SMMs are a promising building block for

* Corresponding Author: Tel.+1 202 767 3413; Fax. +1 202 404 7546; E-mail:pederson@dave.nrl.navy.mil

magnetic storage devices and for investigating macroscopic quantum tunneling[1] and quantum decoherence.[2] A prototype of these SMMs is $[\text{Mn}_{12}\text{O}_{12}(\text{CH}_3\text{COO})_{16}(\text{H}_2\text{O})_4]\cdot 2(\text{CH}_3\text{COOH})\cdot 4(\text{H}_2\text{O})$ (hereafter Mn_{12})[3] which has an effective ground-state spin of $S = 10$. Magnetic hysteresis measurements on the SMM Mn_{12} showed quantum tunneling between spin-up states and spin-down states. [4,5,6,7] This has been successfully explained by magnetic anisotropy parameters only. However, recent measurements on a new type of SMM, $[\text{Mn}_4\text{O}_3\text{Cl}_4(\text{O}_2\text{CEt})_3(\text{py})_3]$ (hereafter Mn_4)[8,9] where $\text{Et}=\text{CH}_2\text{CH}_3$ and $\text{py}=\text{NC}_5\text{H}_5=\text{pyridine}$, showed qualitatively different tunneling behavior[10]: quantum tunneling occurred before the magnetic field was reversed and no quantum tunneling was observed at zero field, which is in contrast to other SMMs like Mn_{12} . It was speculated that this behavior was caused by substantial antiferromagnetic exchange interactions between different monomers within a dimer.[10] Suppose that magnetic moments of all molecules of the SMM Mn_4 are aligned due to strong external magnetic field. If the direction of the external magnetic field is reversed adiabatically through zero field, then some molecules may change their magnetic moments before the external field reversal. This is because the antiferromagnetic exchange interactions facilitate monomeric magnetic moment flips prior to the external field reversal. This interaction also prevents two monomers from simultaneously flipping their magnetic moments at zero field. In contrast, it is widely accepted that for Mn_{12} there are no appreciable exchange interactions between different monomers. In this sense, further investigation of the SMM Mn_4 is worthwhile. Additionally, the SMM Mn_4 consists of the same kinds of Mn spins as those for Mn_{12} but it is much simpler than Mn_{12} since the number of Mn spins is smaller. Therefore the SMM Mn_4 can be used to obtain some insights into issues remaining in the SMM Mn_{12} such as clarifying the origins of symmetry-breaking terms in the effective single-spin Hamiltonian[11,12] and possible spin-orbit-vibron interactions.[13]

A dimeric form of the SMM Mn_4 is obtained by inversion symmetry of the threefold symmetric monomer shown in Fig. 1. Since dimers are well separated from each other, interactions between different dimers are negligible so that they are not considered in our calculations. The magnetic core of the Mn_4 monomer comprises three ferromagnetically coupled Mn^{3+} ($S = 2$) ions coupled antiferromagnetically to the remaining Mn^{4+} ($S = 3/2$) ion leading to a total ground-state spin of $S = 2 \times 3 - 3/2 \times 1 = 9/2$. The core has a similar cubane structure to the inner core of the SMM Mn_{12} , although in Mn_{12} there are four Mn^{4+} ions. In this work, we investigate the electronic structure, magnetic properties, and vibrational modes of the SMM Mn_4 using density-functional theory (DFT).[14] In Sec. 2.1, we present calculations of the Mn_4 monomer such as optimized geometries, intramolecular exchange interactions between Mn spins, and magnetic anisotropy barriers for the ground-state and excited-state manifolds. In Sec. 2.2, we discuss binding energy and exchange interactions between different monomers within a dimer. In Sec. 2.3, we present

calculated infrared and Raman intensities for vibrational normal modes. In Sec. 3, we present our conclusion.

2 DFT calculations and Discussion

We have used all-electron Gaussian-orbital-based Naval Research Laboratory Molecular Orbital Library (NRLMOL) [15,16,17,18,19,20,21] within the Perdew-Burke-Ernzerhof (PBE) generalized gradient approximation (GGA)[22] along with full basis sets for all atoms and fine mesh.[23] In our analysis, we have considered monomers and dimers that are terminated by both H and by the CH_2CH_3 radicals found in the experiments. We have constructed a dimer comprising two conformers of the monomeric units. Our study showed that both conformers are stable. Our vibrational analysis on a monomer terminated by H confirms that there are no unstable modes. The two conformers have slightly different arrangements of the pyridine ligands. The first conformer was found by the density-functional-based optimization of the hydrogenated geometry. It is called the computationally determined conformer (CDC). The second conformer was obtained by the experimental x-ray data with hydrogen positions corrected. This is called the experimentally determined conformer (EDC).

2.1 Monomeric electronic and magnetic properties

Details of finding the CDC monomer were discussed elsewhere[24] so here they are briefly summarized. The Mn_4 monomer has threefold symmetry about the direction of the central bridging Cl-Cl bond in the dimer geometry shown in Fig. 1 (or the direction of connecting Mn^{4+} and Cl in the cubane). To find an initial geometry, we optimize a pyridine ring and a cubane separately. Then the initial geometry for the monomer is relaxed using NRLMOL with the Cl atom fixed to reproduce the experimental Cl-Cl distance upon dimerization. Relaxation continues until maximum forces between atoms are no larger than ~ 0.001 hartree/bohr. A geometry for the dimer can be found by inversion symmetry of the optimized monomer geometry. Charges and magnetic moments for the Mn atoms from the CDC monomer agree well with those from the EDC monomer. The total magnetic moment is $9\mu_B$, which agrees with experiment. The energy gap between the minority lowest unoccupied molecular orbital (LUMO) and the majority highest occupied molecular orbital (HOMO) is much larger than the thermal energy shown in Table 1, so the total magnetic moment of the ground state is stable. Calculated electronic density of states (not shown) confirms that the three Mn^{3+} spins are antiferromagnetically coupled to a Mn^{4+} spin.

Since both the CDC and EDC monomers are stable, we choose one of them, for example, the optimized CDC monomer to examine intramolecular exchange interactions. Considering the symmetry of the monomer and the fact that there are two kinds of Mn spins, we recognize that there are two types of exchange interactions between Mn spins within a monomer as shown in Fig. 2. To calculate the exchange coupling constants, we assume that magnetic moments of all Mn spins are aligned along a particular direction and of Ising type. So a Mn^{3+} spin can have either $M_z = +2$ or $M_z = -2$ and a Mn^{4+} spin can have $M_z = +3/2$ or $M_z = -3/2$. Thus we can construct three different spin configurations other than the ground-state shown in Table 2. For example, $M_s = 15/2$ (M_s is an eigenvalue of the z component of the total spin operator S) is achieved by flipping a Mn^{4+} spin from the ground-state $S = 9/2$: $M_s = 2 + 2 + 2 + 3/2 = 15/2$. Notice that all of the examined spin configurations are not eigenstates of S^2 . We set up geometries of the three spin configurations using the optimized ground-state geometry with corresponding Ising-type spin arrangements and proper magnetic moments. Then we minimize self-consistently the energies of the spin configurations. Comparing the energies of the three configurations (refer to Table 2) with the energy gap between the minority LUMO and the majority HOMO, we find that the examined spin configurations have an order of magnitude smaller energy than other kinds of spin excitations such as moving one majority spin to the unoccupied minority orbital. So we call those spin configurations low-energy spin excitations. Since there are three unknowns (the background energy, E_0 , the two types of exchange constants, J_1 and J_2) and four equations to solve, we can calculate the exchange constants by the least-square-fit (LSF) method. Our calculated values of J_1 and J_2 are presented in Table 3.

Differences between the calculated energies and the LSF-determined values for the ground state and low-energy spin excitations are quite small as shown in Table 2. The exchange constant between Mn^{3+} spins, J_1 , is confirmed to be ferromagnetic, and the exchange constant between Mn^{3+} spins and a Mn^{4+} spin, J_2 , is antiferromagnetic but larger than J_1 . From exact diagonalization of Heisenberg exchange Hamiltonian, we confirm that the ground-state manifold has $S = 9/2$, that the first excited-state manifolds are doubly degenerate with $S = 7/2$, and that the second excited-state manifold has $S = 11/2$. The energy gaps between the ground-state manifold and the excited-state manifolds are given in Table 3. The large energy gap between the ground-state and the first-excited manifold also supports that the ground-state $S = 9/2$ manifold is stable. To check how good the calculated values of J_1 and J_2 are compared to experiment, we calculate the effective moment per molecule, μ_{eff} , at magnetic field of 1 T as a function of temperature T as follows:

$$\mu_{\text{eff}} = \frac{\sqrt{3\chi k_B T}}{\mu_B} \quad (1)$$

where χ is susceptibility, k_B is the Boltzmann constant, and μ_B is the Bohr magneton. If we use the calculated values of J_1 and J_2 given in DFT(1) of Table 3, then we obtain overestimated effective moments (dashed curve in Fig. 3) at high temperatures compared to the experimental data. If we use half-reduced values of J_1 and J_2 from the DFT-calculated ones, then the calculated effective moment (solid curve in Fig. 3) agrees well with experiment. Notice that the reduced values of J_1 and J_2 are quite close to the experimentally extracted values in Table 3. This supports the argument that DFT calculations often overestimate the exchange interactions between atoms because of imperfect treatment of self-interaction of the Coulomb potential.

We calculate the magnetic anisotropy barrier (MAE) in zero magnetic field for both the CDC and EDC monomers for the ground state $S = 9/2$, assuming that the spin-orbit coupling mainly contributes to the barrier. Following the procedure explained in Ref. [25], we find that the Mn_4 monomer has the easy axis along the threefold axis, in agreement with experiment. The calculated anisotropy barrier is about 11.3 K for the CDC monomer, 11.6 K for the EDC monomer, and 10.9 K for the hydrogenated EDC monomer. All of these values are close to the experimentally measured value of 14.4 K. To investigate the contribution of each Mn spin to the barrier, we project the total barrier onto each Mn spin and calculate its projected anisotropy. The three Mn^{3+} spins have the easy axes along the x , y , and z axis respectively. The Mn^{4+} spin has the easy axis along the $\langle 111 \rangle$ direction. Most of the anisotropy originates from the Mn^{3+} spins due to Jahn-Teller distortion, while the contribution of the Mn^{4+} spin is insignificant. The same tendency occurs for the SMM Mn_{12} . We also calculate the magnetic anisotropy barriers for the low-energy spin excitations shown in Table 2. The barriers are essentially the same as that for the ground state $S = 9/2$.

2.2 Dimeric properties

For a dimeric form, the distance between the central bridging Cl-Cl bond is kept as the experimental value of 3.86 Å unless specified. We calculate the binding energy of the dimer by subtracting the dimer energy from twice the monomer energy. We find that the dimer is stable for both the CDC and EDC. For the CDC (hydrogenated EDC) dimer, the binding energy is about 0.16 eV (0.45 eV). [24] The magnitude of the binding energy suggests attractive electrostatic interactions between different monomers. We find that the electric dipole moment for each CDC (hydrogenated EDC) monomer is as large as 2.28 (1.91) in atomic units and that it points towards the Cl atom in the cubane along the threefold axis. Since the dimer has inversion symmetry, the electric dipole moment for the dimer vanishes. The discrepancy between the binding energy for the CDC and that for the EDC arises from our substitution of

CH₂CH₃ for H and slightly different geometries of pyridine rings for both conformers.

To calculate the exchange coupling constant J_{inter} between different monomers within a dimer, we make assumptions that a monomer is an ideal $S = 9/2$ object and that its effective spin is aligned along the easy axis and of Ising type (either $M_z = +9/2$ or $M_z = -9/2$). Then we calculate self-consistently the energies of ferromagnetic (parallel monomeric spins) and antiferromagnetic (antiparallel monomeric spins) configurations of the dimer, and take the difference δ between the two energies. We find that the antiferromagnetic configuration is favored, and that from $\delta = 2J_{\text{inter}}(9/2)^2$ the exchange constant J_{inter} is about 0.24 K for the CDC and 0.27 K for the EDC.[24] This can be compared to the experimentally measured value of 0.1 K. From the analysis of the exchange constants within a monomer, this overestimated value of J_{inter} is not so surprising. We also find that J_{inter} is quite sensitive to the central bridging Cl-Cl bond length. Our calculations show that J_{inter} increases exponentially with decreasing the Cl-Cl distance. More detailed analysis was given in Ref.[24]. Since the experimental results cannot distinguish exchange interaction from magnetic dipole-dipole interaction, we estimate the contribution of the magnetic dipole-dipole interaction to the total interactions between different monomers in a dimeric form. Since the dipole moment is along the easy axis and the two monomers are located along the easy axis, the ferromagnetic configuration is favored. But the difference in the dipole-dipole interaction between the ferromagnetic and antiferromagnetic configuration is about 0.28 K, which is negligible compared to the exchange energy difference of 10 K. This was calculated considering two large spins of $S = 9/2$. Including the internal structure of a monomer does not substantially change the energy difference in the dipole-dipole interaction.

2.3 Vibrational analysis

We calculate vibrational normal modes for the EDC monomer with CH₂CH₃ substituted by H within the harmonic oscillator approximation. There are a total of 168 normal modes ($= 56 \times 3$), six of which are translational and rotational modes. All of these modes are vibrationally stable, which is also corroborated by our frozen phonon calculations. Based on the normal coordinates obtained from the vibrational analysis, we investigate which modes are infrared (IR) and/or Raman active. IR absorption intensity is proportional to the square of change of electric dipole moment with respect to displacement along the normal coordinates. Raman scattering intensity is proportional to square of the change of polarizability with respect to displacement along the normal coordinates. We calculate the IR absorption and Raman scattering intensities following the method suggested in Ref. [21,26,27,28]. First, we discuss the IR spectra

shown in Fig. 4. Projection of the total IR intensities onto each component in the monomer, indicates which component contributes to the spectra at certain modes. Overall, we find four strong IR intensities at 543 cm^{-1} , 1316 cm^{-1} , 1547 cm^{-1} , and 2942 cm^{-1} . For low-frequency modes below 444 cm^{-1} all parts of the monomer contribute. At 543 cm^{-1} , the dominant contributions are from O^{2-} and Mn. The contributions of Mn and O^{2-} are limited to low-frequency modes (below 602 cm^{-1}). From 671 cm^{-1} the contribution from pyridine rings becomes important. At 1316 cm^{-1} , 1547 cm^{-1} , 1563 cm^{-1} , and 2942 cm^{-1} the contributions are from O_2CH and pyridine rings. For high-frequency modes the vibrations of O_2CH and pyridine rings provide dominant IR intensities. Second, we discuss the Raman spectra shown in Fig. 5. The Raman intensities are strong mostly at very low vibrational frequencies, in contrast to the IR intensities that are strong at high frequencies. The strongest Raman intensity is at 21 cm^{-1} , and the next largest peak is at 35 cm^{-1} . These modes are mainly due to vibrations of pyridine rings as well as small contributions from Cl, Mn, and O_2CH . At 76 cm^{-1} and 96 cm^{-1} the dominant contributions are from Cl and smaller ones from pyridine, O_2CH , and Mn. At 111 cm^{-1} , 168 cm^{-1} , and 212 cm^{-1} , the contributions are from all components except for O^{2-} . At 514 cm^{-1} , 543 cm^{-1} , and 602 cm^{-1} the contributions are from O^{2-} and Mn only. At 1019 cm^{-1} , only pyridine rings contribute, and at 2942 cm^{-1} (not shown) O_2CH and pyridine rings contribute. At 3115 cm^{-1} , 3132 cm^{-1} , and 3154 cm^{-1} (not shown) only pyridine rings contribute. Compared to the IR spectra, the contributions of Cl atoms are noticeable for low-frequency modes and those of O^{2-} appear at between 514 cm^{-1} and 602 cm^{-1} only. For high-frequency modes, the contributions are from pyridine and O_2CH only.

3 Conclusion

We have found optimized geometries for the Mn_4 monomer and dimer using DFT, and calculated exchange interactions between Mn spins within the monomer and magnetic anisotropy barriers for the ground state $S = 9/2$ and the low-energy spin excitations. We also have calculated the binding energy and the monomer-monomer exchange interaction and magnetic dipole-dipole interaction within a dimer. Most of our DFT calculations are in good agreement with experiment, although the calculated intermolecular/intramolecular exchange interactions are somewhat overestimated compared to the experimental values as is common for DFT calculations. Our vibrational analysis on the hydrogenated EDC monomer rules out a possibility of breaking the threefold symmetry by stable soft vibrational modes in the SMM Mn_4 . The calculated IR and Raman spectra can be checked by experiments.

Acknowledgments

KP was funded by W. M. Keck Foundation, MRP and NB were supported in part by ONR and NRL. Computer time was provided by the DoD HPCMPO at the ERDC MSRC.

References

- [1] E. M. Chudnovsky, J. Tejada, Macroscopic Quantum Tunneling of the Magnetic Moment, Cambridge Studies in Magnetism, vol. 4, Cambridge University Press, Cambridge, 1998.
- [2] P. C. E. Stamp, I. S. Tupitsyn, cond-mat/0302015 (unpublished).
- [3] T. Lis, Acta Crystallogr. B 36 (1980) 2042.
- [4] R. Sessoli, D. Gatteschi, A. Caneschi, M.A. Novak, Nature (London) 365 (1993) 141.
- [5] J. R. Friedman, M. P. Sarachik, J. Tejada, R. Ziolo, Phys. Rev. Lett. 76 (1996) 3830.
- [6] A. L. Barra, D. Gatteschi, R. Sessoli, Phys. Rev. B 56 (1997) 8192.
- [7] J. A. A. J. Perenboom, J. S. Brooks, S. Hill, T. Hathaway, N. S. Dalal, Phys. Rev. B 58 (1998) 330.
- [8] D. N. Hendrickson, G. Christou, E. A. Schmitt, E. Libby, J. S. Bashkin, S. Wang, H. -L. Tsai, J. B. Vincent, P. D. W. Boyd, J. C. Huffman, K. Folting, Q. Li, W. E. Streib, J. Am. Chem. Soc. 114 (1992) 2455.
- [9] R. S. Edwards, S. Hill, S. Bhaduri, N. Aliaga-Alcalde, E. Bolin, S. Maccagnano, G. Christou, D. N. Hendrickson, accepted for publication in Polyhedron.
- [10] W. Wernsdorfer, N. Aliaga-Alcalde, D. N. Hendrickson, G. Christou, Nature, 416 (2002) 406.
- [11] E. M. Chudnovsky, D. A. Garanin, Phys. Rev. Lett. 87 (2001) 187203.
- [12] A. Cornia, R. Sessoli, L. Sorace, D. Gatteschi, A. L. Barra, C. Daiguebonne, Phys. Rev. Lett. 89 (2002) 257201.
- [13] M. R. Pederson, N. Bernstein, J. Kortus, Phys. Rev. Lett. 89 (2002) 97202.
- [14] W. Kohn, L. J. Sham, Phys. Rev. 140 (1965) A1133.
- [15] M. R. Pederson, K. A. Jackson, Phys. Rev. B 41 (1990) 7453.
- [16] K. A. Jackson, M. R. Pederson, Phys. Rev. B 42 (1990) 3276.

- [17] M. R. Pederson, K. A. Jackson, Phys. Rev. B 43 (1991) 7312.
- [18] A. Briley, M. R. Pederson, K. A. Jackson, D. C. Patton, D. V. Porezag, Phys. Rev. B 58 (1998) 1786.
- [19] A. A. Quong, M. R. Pederson, J. L. Feldman, Solid State Commun. 87 (1993) 535.
- [20] D. V. Porezag, Ph.D. thesis, Chemnitz Technical Institute, 1997.
- [21] D. Porezag, M. R. Pederson, Phys. Rev. B 54 (1996) 7830.
- [22] J. P. Perdew, K. Burke, M. Ernzerhof, Phys. Rev. Lett. 77 (1996) 3865.
- [23] D. Porezag, M. R. Pederson, Phys. Rev. A 60 (1999) 2840.
- [24] K. Park, M. R. Pederson, S. L. Richardson, N. Aliaga-Alcalde, G. Christou, cond-mat/0303645 (unpublished).
- [25] M. R. Pederson, S. N. Khanna, Phys. Rev. B 60 (1999) 9566.
- [26] E. B. Wilson, J. C. Decius, P. C. Cross, Molecular Vibrations McGraw-Hill, New York, 1955.
- [27] M. Cardona, in: M. Cardona, G. Güntherodt (Eds)., Light Scattering in Solids, vol. 50, Springer-Verlag, Berlin, 1982.
- [28] W. F. Murphy, W. Holzer, H. J. Bernstein, Appl. Spectrosc. 23 211 (1969) 211.

Table 1

Energy gaps between the highest occupied molecular orbital (HOMO) and the lowest unoccupied molecular orbital (LUMO) for majority and minority spins for the SMM Mn₄ monomer.

maj HOMO - maj LUMO	min HOMO - min LUMO
1.02 eV	2.42 eV
min LUMO - maj HOMO	maj LUMO - min HOMO
1.17 eV	2.28 eV

Table 2

Eigenvalues of the z component of the total spin operator, M_s , spin configurations, their Ising exchange energies, calculated energies relative to the ground state energy, ΔE , differences between the calculated and the least-square-fitted energies, and calculated magnetic anisotropy barriers (MAE) per monomer for the ground state and the low-energy spin excitations. For the spin configurations, the first three symbols are for the three Mn³⁺ spins ("+" denotes $M_z = +2$) and the fourth one is for the Mn⁴⁺ spin ("+" denotes $M_z = +3/2$). Here E_0 is the background energy, J_1 and J_2 are the intramolecular exchange constants indicated in Fig. 2. These calculations were performed for a computationally determined conformer (CDC).

M_s	spin conf.	Ising energy	ΔE (eV)	$E^{\text{DFT}} - E^{\text{LSF}}$ (eV)	MAE/monomer (K)
9/2	+ + + -	$E_0 + 12J_1 - 9J_2$	0	-2.7×10^{-4}	11.3
1/2	+ + - -	$E_0 - 4J_1 - 3J_2$	0.14	8×10^{-4}	11.4
7/2	+ + - +	$E_0 - 4J_1 + 3J_2$	0.217	-8×10^{-4}	11.8
15/2	+ + + +	$E_0 + 12J_1 + 9J_2$	0.236	2.7×10^{-4}	10.9

Table 3

Calculated intramolecular exchange constants, energy gap between the ground-state $S = 9/2$ and the first excited doubly degenerate $S = 7/2$ manifold, $E(S = 7/2)$, and energy gap between the ground-state and the second-excited $S = 11/2$ manifold, $E(S = 11/2)$, in comparison with the experimental results.[8,10] The negative sign means ferromagnetically coupled. DFT(1) denotes our calculated values, while DFT(2) denotes values obtained by reducing our calculated values by half. The last two columns are the binding energy and intermolecular exchange constant within a CDC dimer.

	J_1 (K)	J_2 (K)	$E(S = \frac{7}{2})$ (K)	$E(S = \frac{11}{2})$ (K)	Binding energy (eV)	J_{inter} (K)
DFT(1)	-44	152	490	836	0.16	0.24
DFT(2)	-22	76	245	418		
Exp	-25[8]	60[8]	238[8]	330[8]		0.1[10]

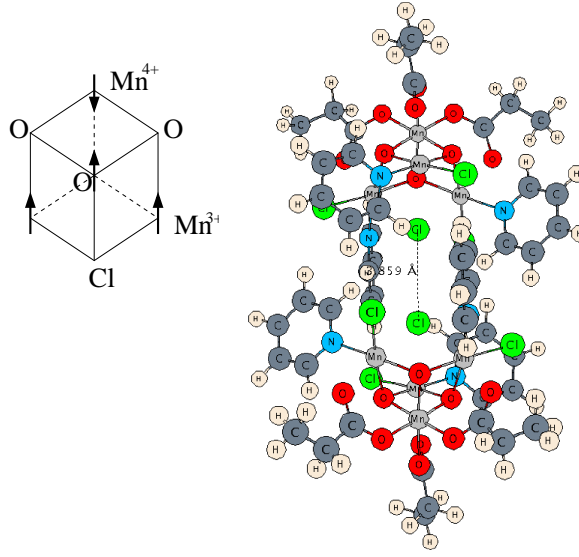


Fig. 1. (Left) Cubane-like magnetic core of the Mn_4 monomer. The four arrows represent Mn spins and O and Cl atoms are labeled. The magnetic core consists of three ferromagnetically coupled Mn^{3+} spins ($S=2$) coupled antiferromagnetically to one Mn^{4+} spin ($S=3/2$) ion leading to a total spin of $S = 9/2$. (Right) Mn_4 dimer geometry. The dimer is formed by inversion of the threefold symmetric monomer. The distance between the two central Cl atoms marked as the dotted line was measured to be 3.86 Å. The threefold axis is along this Cl-Cl bond.

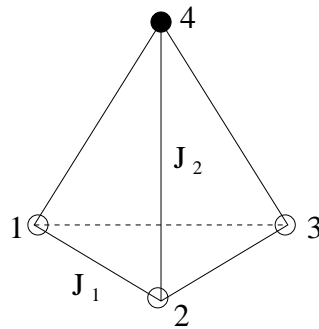


Fig. 2. Schematic diagram of intramolecular exchange interactions within a monomer. Three Mn^{3+} ($S = 2$) spins are denoted as empty circles and one Mn^{4+} ($S = 3/2$) spin as a filled circle at the four vertices of the tetrahedra. Each spin is numerically labeled at each vertex. J_1 is the exchange interaction between Mn^{3+} spins and J_2 is between Mn^{3+} and Mn^{4+} spins.

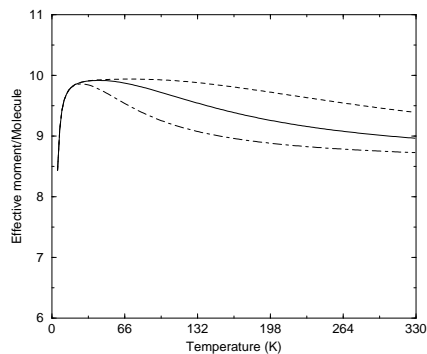


Fig. 3. Calculated effective moment μ_{eff} per monomer. The dashed, solid, and dot-dashed curves are obtained using the calculated values of J_1 and J_2 , a half of the calculated values, and a quarter of the calculated values respectively. The solid line is close to the experimental data.[8]

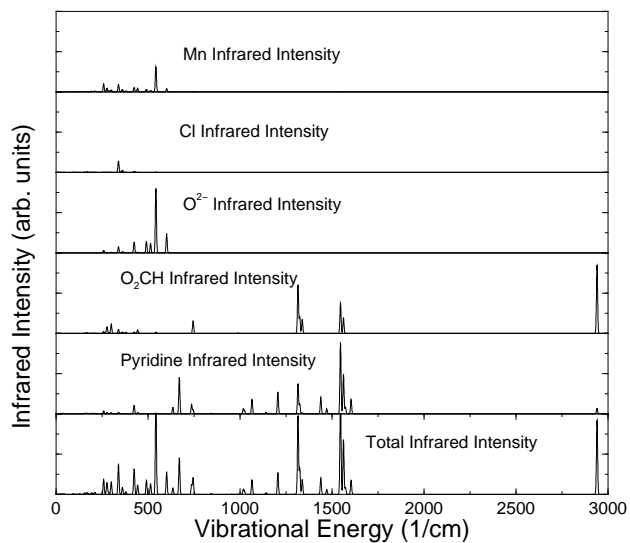


Fig. 4. Calculated total and projected infrared (IR) vibrational spectra for the experimentally determined conformer (EDC) with CH_2CH_3 replaced by H. From the top panel, shown are the projected IR active density of states onto Mn, Cl, O^{2-} , O_2CH , and pyridine ligands, and the total IR density of states. All of the projected IR density of states have the same scale as the total IR density of states.

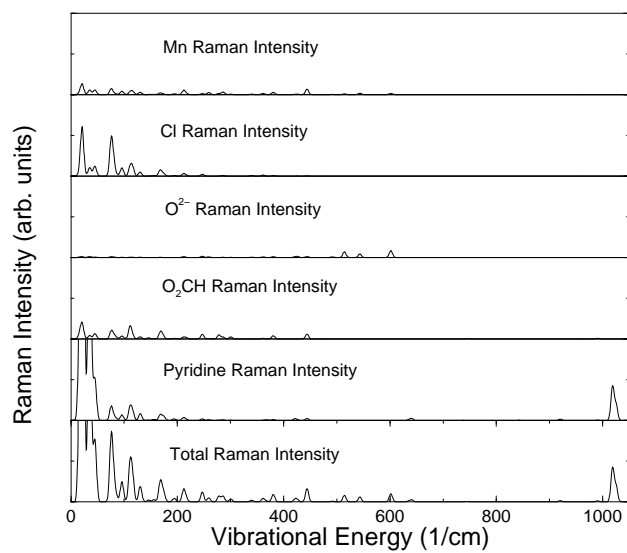


Fig. 5. Calculated total and projected Raman vibrational spectra for the same monomer used for the IR spectra. All of the projected Raman intensities have the same scale as the total Raman intensity.